

<https://doi.org/10.1038/s41612-025-01079-9>

Heterogeneity in ice sheets- vs. monsoon rainfall-induced silicate weathering from high to low latitudes



Xuguang Feng^{1,2,3}, Jianjun Zou^{1,2,3}, Xuefa Shi^{1,2,3}✉, Zhengyao Lu⁴✉, Hai Cheng⁵, Yi Zhong⁶, Zhengquan Yao^{1,2,3}, Zhaojie Yu^{2,7}, Hanying Li⁵, Zhi Dong^{1,2,3}, Debo Zhao^{2,7}, Han Feng^{1,2,3}, Jiang Dong^{1,2,3} & Kunshan Wang^{1,2,3}

One of the most challenging problems in paleoclimate research is how orbital cyclicities forced Earth's climate variations during the late Quaternary. To address this issue, we investigated the differences in silicate weathering, a sensitive climate indicator, at different latitudes on orbital timescales by examining geochemical and clay mineral data from the mid-latitude Sea of Okhotsk and integrating published weathering records from low to high latitudes. Results show that silicate weathering in the mid-latitude Sea of Okhotsk responded sensitively to both temperature and rainfall, indicating the combined influence of ice sheets and low-latitude monsoons. However, silicate weathering is more sensitive to temperature in high-latitude regions, and to rainfall in tropical areas. Therefore, ice sheets primarily control silicate weathering at high latitudes, whereas monsoon rainfall has greater influences in tropical areas. These findings seem to support the “Milankovitch–Kutzbach” hypothesis, which proposes that ice sheets and monsoons together control orbital-scale climate variations of Earth.

The widely accepted “Milankovitch theory” argues that the Northern Hemisphere (NH) 65°N summer insolation induces the waxing and waning of ice sheets and affects the global climate on orbital timescales¹, and this theory has been corroborated by numerous studies on marine^{2–4}, ice core⁵, loess⁶, and lake records⁷. However, this theory does not adequately explain many paleoclimate records in low-latitude regions^{8,9}. In the vast low-latitude region (~30°N to ~30°S), which covers half of the Earth's surface, the amount of solar energy received is an order of magnitude greater than that received above 65°N^{9,10}. Low-latitude interhemispheric insolation gradients have been proposed to drive global monsoon rainfall patterns and have resulted in many paleoclimate records (e.g., speleothem $\delta^{18}\text{O}$, Loess ¹⁰Be flux, and so on) related to hydrological cycles in low-latitude regions that exhibit clear precession cycles (23-kyr), independent of high-latitude ice sheet changes (characterized by dominant 100-kyr cycles)^{8,9,11,12}. Moreover, Cheng et al.⁹ recently proposed a novel perspective on climate changes occurring on orbital timescales, known as the “Milankovitch–Kutzbach” hypothesis. This hypothesis suggests that Earth's climate variations on orbital scales are primarily driven by the combination of ice sheets at high

latitudes and monsoon systems at low latitudes. However, which mechanism could better explain climate variations on the orbital scale—namely, high-latitude ice sheets, low-latitude monsoons, or a combination of high-latitude ice sheets and low-latitude monsoons—deserves further study.

Silicate weathering, an essential process that occurs at the Earth's surface, is highly sensitive to climate change^{13,14}. Modern observations of surface soils and river sediments have confirmed a linear relationship between climate parameters (e.g., temperature and rainfall) and weathering intensity^{15–17}. A warm and wet climate promotes chemical weathering and causes the leaching and mobilization of mobile elements (e.g., Na, K, Ca, and Mg), as well as the transformation of primary minerals into secondary mineral phases¹⁸. Consequently, the accumulation and preservation of weathering products have been utilized to investigate weathering processes associated with climate change on tectonic^{17,19}, orbital^{13,20}, and millennial timescales^{21,22}. On orbital timescales, the influences of high-latitude ice sheets and low-latitude monsoons on climate systems are markedly disparate⁹. High-latitude ice sheets drive global temperature variations following similar patterns on the glacial-interglacial scale²³, which are

¹Key Laboratory of Marine Geology and Metallogeny, First Institute of Oceanography, Ministry of Natural Resources, Qingdao, 266061, China. ²Laboratory for Marine Geology, Qingdao Marine Science and Technology Center, Qingdao, 266237, China. ³Key Laboratory of Deep Sea Mineral Resources Development, Shandong (Preparatory), Qingdao, 266061, China. ⁴Department of Physical Geography and Ecosystem Science, Lund University, Sölvegatan 12, 22362 Lund, Sweden. ⁵Institute of Global Environmental Change, Xi'an Jiaotong University, Xi'an, 710049, China. ⁶Advanced Institute of Ocean Research, Southern University of Science and Technology, Shenzhen, 518055, China. ⁷Key Laboratory of Marine Geology and Environment, Institute of Oceanology, Chinese Academy of Sciences, Qingdao, 266071, China. ✉e-mail: xfshi@fio.org.cn; zhengyao.lu@nateko.lu.se

characterized by 100-kyr cycles, whereas low-latitude monsoons mainly regulate the tropical hydrological cycle, which is characterized by 23-kyr cycles^{9,24}. Given the sensitivity of silicate weathering to fluctuations in temperature and rainfall, the dominant periods observed in weathering records can illuminate key climatic driving mechanisms. Specifically, the primary 100-kyr cycles suggest that silicate weathering is strongly modulated by high-latitude ice sheet dynamics (temperature-driven), and the dominant 23-kyr precession signal implies a central role for monsoon rainfall in regulating weathering rates. The co-occurrence of both 100- and 23-kyr cycles in weathering records points to dual control by high-latitude ice sheets and low-latitude monsoons. Hence, by analyzing latitudinal variations in silicate weathering and their linkages to temperature and rainfall, we can disentangle the relative contributions of high-latitude ice sheets and low-latitude hydroclimate to weathering feedback, which offers a framework to unravel the orbital-scale climate variations of Earth.

Various proxies have been used to evaluate the intensity of chemical weathering in source regions^{25–27}. Among these proxies, clay mineralogy and geochemical signatures have proven to be the most effective in evaluating weathering patterns and investigating spatial and temporal climate change across extensive continental regions^{28,29}. In this study, we utilized element

proxies (chemical index of alteration (CIA), modified CIA (CIX), and K/Al) and a mineral proxy (smectite/illite) at Site LV55-38-3 (48°40'N, 146°57'E, water depth: 1026 m) in the Sea of Okhotsk (Figs. 1 and S1) to reconstruct the weathering intensity in mid-latitude sediment sources (Supplementary Text S1 and Figs. S2–S9). We also compiled published weathering records from other regions, including K/Ti ratios from the high-latitude Bering Sea, K/Al ratios from the low-latitude Gulf of Guinea, and smectite/(illite + chlorite) ratios from the low-latitude Bay of Bengal^{20,30–34} (Supplementary Text S2 and Fig. S10). These weathering records span wide geographic coverage from low to high latitudes (Fig. 1) and provide insights into climate evolution and its driving mechanisms on orbital timescales.

Results and discussion

Heterogeneity in silicate weathering records from high to low latitudes

Overall, there are obvious discrepancies in the weathering records from high to low-latitude regions on orbital timescales (Fig. 2). In the mid-latitude Sea of Okhotsk, the weathering records at Site LV55-38-3 have clear glacial-interglacial cycles, with notable 100- and 41-kyr periods (Figs. 2d, e and S11). Glacial intervals are characterized by reduced

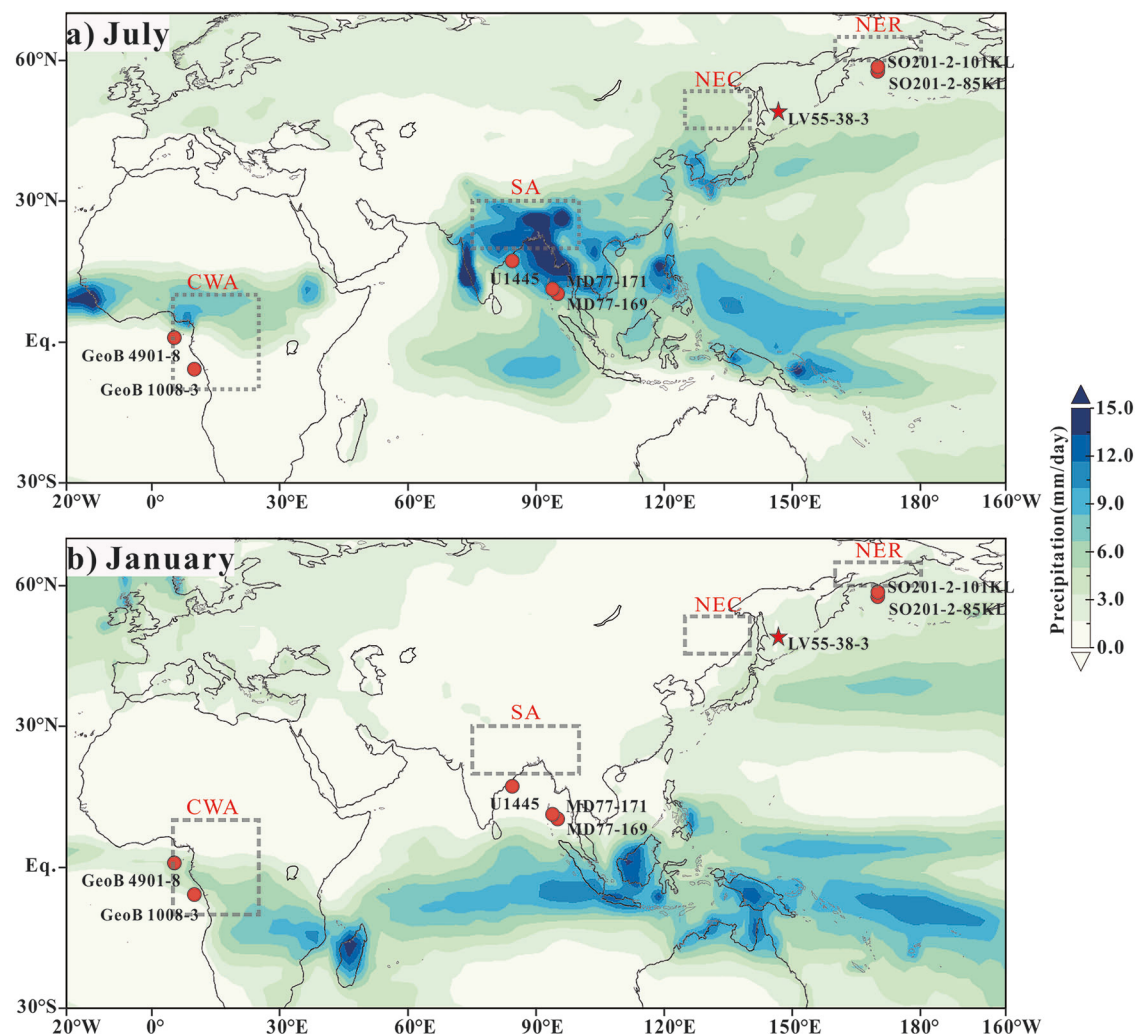


Fig. 1 | Present-day precipitation between 30°S and 70°N. Maps showing the mean (1981–2010) CMAP global precipitation rates during July (a) and January (b). The precipitation distribution reflects monsoon development. The red stars represent the proxy records generated in this study. The red circles represent proxy records collected from previous studies. The precipitation data are available from <https://psl.noaa.gov/data/gridded/data.cmap.html>. The maps were produced using Panoply (source: <https://www.giss.nasa.gov/tools/panoply/>). We also chose four regions to

simulate the rainfall variability over the past 240 ka, and these four regions were considered the sediment sources for the study sites. Northeast Russia (NER, 60–65°N, 160–180°E), Northeast China (NEC, 46–53°N, 120–140°E), South Asia (SA, 15–30°N, 75–100°E), and Central West Africa (CWA, 10°S–10°N, 5–25°E). Additionally, we chose the 3 months with the highest rainfall during the year to reflect rainfall variability in the study region.

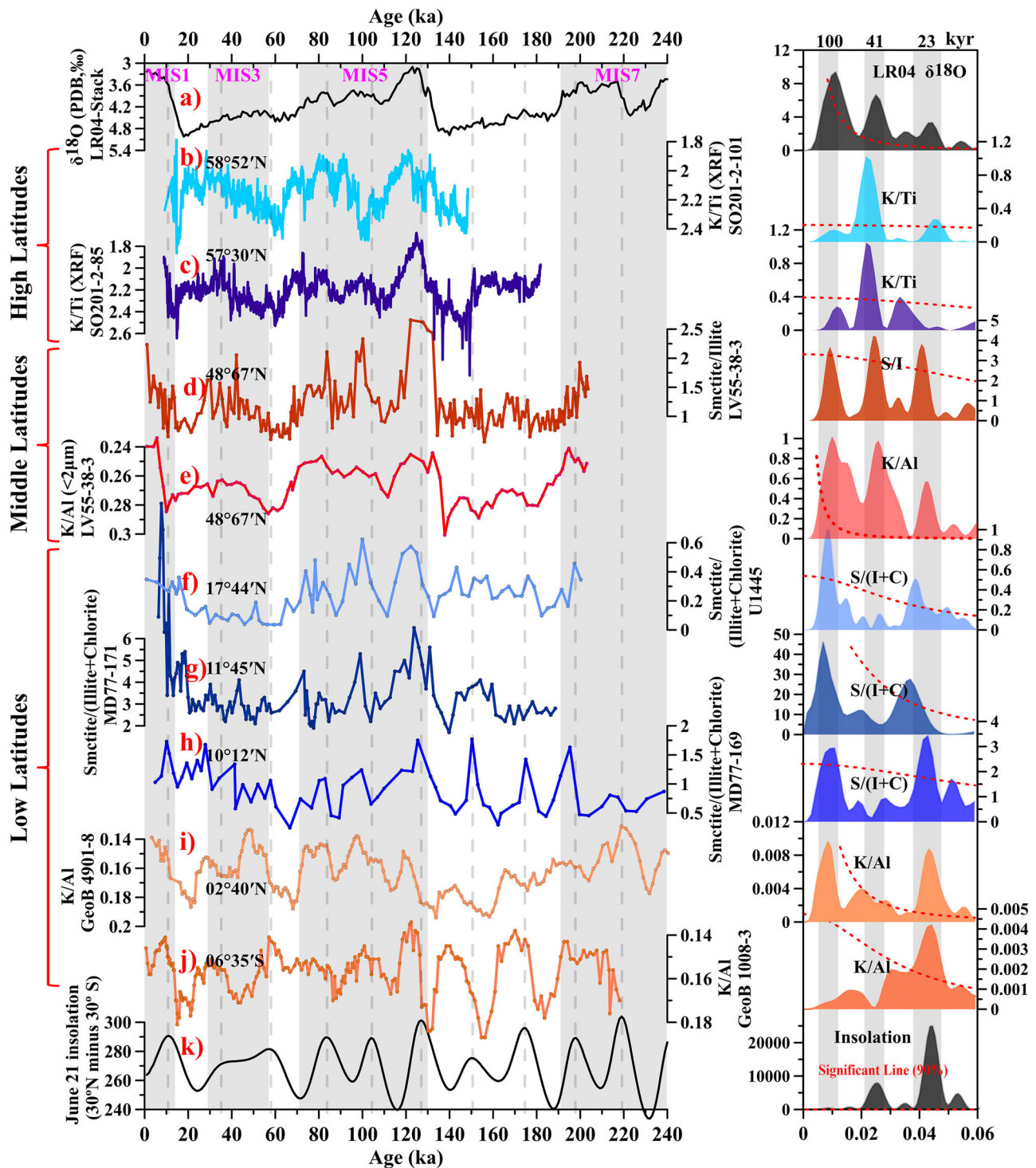


Fig. 2 | Weathering records from high to low latitudes and their corresponding spectral analysis results (right). a 57 stacked, globally distributed benthic $\delta^{18}\text{O}$ records (LR04 stack)⁴, **(b)** K/Ti ratio (XRF) from Site SO201-2-101KL³⁰, **(c)** K/Ti ratio (XRF) from Site SO201-2-85KL³⁰, **(d)** Smectite/illite ratio from Site LV55-38-3 (this study), **(e)** K/Al ratio from Site LV55-38-3 (this study), **(f)** Smectite/(illite +

chlorite) ratio from Site U1445³¹, **(g)** Smectite/(illite + chlorite) ratio from Site MD77-171²⁰, **(h)** Smectite/(illite + chlorite) ratio from Site MD77-169³², **(i)** K/Al ratio from Site GeoB 4901-8³³, **(j)** K/Al ratio from Site GeoB1008-3³⁴, **(k)** June 21 insolation differential between 30°N and 30°S¹⁰. Notes: In the spectral analysis, the red dotted lines indicate the 90% significance level.

smectite/illite ratios, lower CIA and CIX values, and elevated K/Al ratios, whereas interglacial periods have significantly increased smectite/illite ratios, higher CIA and CIX values, and decreased K/Al ratios. These trends reflect intensified mineral transformation and enhanced leaching of mobile elements during interglacials, indicating higher weathering rates in mid-latitude regions under warmer conditions. In particular, beyond glacial-interglacial variability, the Site LV55-38-3 weathering

records also display pronounced precession-driven cycles (23-kyr, Figs. 2d, e and S11), which closely align with low-latitude summer insolation. In the high-latitude Bering Sea, the weathering proxy K/Ti ratio at two sites (SO201-2-85KL and SO201-2-101KL) also shows distinct glacial-interglacial cycles but with weaker 23-kyr cycles (Fig. 2b, c). Glacial periods show elevated K/Ti ratios reflecting reduced weathering intensity, contrasting with lower ratios during interglacial periods that indicate

enhanced weathering. Here, owing to the relatively short timescales covered by the two Bering Sea cores, spectral analysis of K/Ti ratios shows no significant power at 100-kyr cycles, with prominent power only at the 41-kyr band. In contrast to the marked glacial-interglacial fluctuations observed at middle and high latitudes, weathering records from the Bay of Bengal and the Gulf of Guinea at low latitudes show stronger 23-kyr precession signals that closely track the pattern of low-latitude insolation (Fig. 2f–j). Although spectral analysis also reveals 100-kyr cycles in the weathering records (smectite/(illite + chlorite)) from the Bay of Bengal, it seems like these records exhibit a more pronounced precession-band (23-kyr) signal, particularly during glacial intervals (Fig. 2f–h). This demonstrates that silicate weathering in the low-latitude Bay of Bengal was primarily governed by precession forcing. Overall, our results demonstrate that weathering records in middle latitudes exhibit not only pronounced glacial-interglacial variability (100-kyr cycles) but also distinct precession (23-kyr) cycles. In contrast, high-latitude weathering records are dominated by strong glacial-interglacial fluctuations, whereas low-latitude weathering records primarily reflect robust 23-kyr cycles. Notably, the intensity of the 23-kyr signal in weathering records progressively increases from high to low latitudes, whereas the strength of the 100-kyr signal systematically decreases (Fig. 2).

Forcing mechanism of silicate weathering from high to low latitudes

Mid-latitude regions. Previous studies have systematically analyzed the factors influencing silicate weathering, including lithology, topography, and climate (temperature and rainfall (related to runoff))^{35–38}. Among them, runoff and lithology have been identified as the strongest predictors of chemical weathering rates^{35–38}. Increased rainfall typically leads to higher runoff, which enhances water-rock interactions through both increased contact time and greater availability of acidic solutions, thereby accelerating mineral dissolution^{36–38}. The sediments at Site LV55-38-3 are predominantly derived from the Amur River (Supplementary Text S1 and Figs. S4 and S7), which is situated in Northeast China. This region lies within the marginal zone of the East Asian Summer Monsoon (EASM)³⁹, and the pronounced variations in EASM intensity over the past 200 kyr would have substantially influenced regional rainfall patterns, thereby affecting silicate weathering. Furthermore, mafic rocks such as basalt, which are rich in soluble minerals, present weathering rates that are 5–10 times higher than those of granitic rocks⁴⁰, whereas quartz-rich rocks such as sandstone present much lower rates because of the resistance of quartz to weathering³⁶. However, provenance analysis of Site LV55-38-3 revealed no substantial changes in sediment sources over the past 200 kyr, with the Amur River remaining the dominant contributor (Figs. S4, S6 and S7), suggesting that lithological effects on silicate weathering may have been negligible in our study. Moreover, a recent global compilation of modern sediment datasets revealed that as temperature decreases because of increasing latitude, silicate weathering intensity significantly weakens, highlighting the crucial role of temperature on silicate weathering⁴¹. Notably, we collected sea surface temperatures (SST) in the mid-to-high-latitude regions of the NH^{42–45} (~30°–60°N, Fig. S12), and the temperature variability could reach 8–12 °C across glacial-interglacial cycles (Figs. 3g and S13). Therefore, the potential influence of temperature on silicate weathering can not be overlooked in the mid-latitude regions. As mentioned above, temperature variability is primarily driven by high-latitude ice sheet dynamics, and rainfall is strongly influenced by low-latitude monsoon systems. Our study area lies at the confluence of ice sheets and monsoon influences. Therefore, the analysis of weathering records in the context of temperature and rainfall variability will yield critical insights into how ice sheet dynamics and monsoon systems regulate mid-latitude weathering processes.

As illustrated in Figs. 3g and S13, the compiled average SST of the mid-to-high-latitude regions of the NH exhibits pronounced glacial-interglacial cycles, dominated by 100-kyr periodicity. These variations align closely with the weathering records at Site LV55-38-3 (Fig. 3e). During interglacial

periods, elevated SST coincides with markedly increased weathering rates, whereas glacial intervals show suppressed weathering under cooler conditions. Cross-spectral analysis further confirmed strong coherence between SST and weathering proxies in the 100-kyr band (Fig. S14). Critically, interglacial SST at middle to high latitudes was approximately 8–12 °C higher than those recorded during glacial periods (Figs. 3g and S13)—a magnitude of temperature change that, based on modern sediment data across latitudes⁴¹, would drive substantial shifts in weathering intensity. Our results thus demonstrate that mid-latitude silicate weathering is sensitive to temperature variability at glacial-interglacial timescales.

Notably, the weathering proxies at Site LV55-38-3 also display significant precession cycles (23-kyr; Figs. 3e and S11), which are weakly observed in the SST records (Fig. 3g). Precession signals appear mainly in low-latitude monsoon records and are closely related to the water vapor cycle at low latitudes^{8,9,46,47}. As illustrated in Fig. 3c, d, both simulated rainfall in Northeast China (sediment source of the Sea of Okhotsk) and East Asian rainfall reconstructions derived from Chinese speleothem $\delta^{18}\text{O}$ exhibit pronounced precession cycles (23-kyr). Within this band, weathering proxies display a robust positive correlation with rainfall variability, with elevated rainfall consistently corresponding to enhanced silicate weathering (Fig. S15). Cross-spectral and cross-wavelet analyses further confirmed their in-phase coupling, underscoring a tight link between hydroclimate dynamics and weathering rates (Figs. S14 and S16). Mechanistically, intensified EASM facilitates the transport of more moisture from the tropical Pacific Ocean to the interior of East Asia, increasing regional rainfall. This elevated rainfall accelerates the process of mineral dissolution by transporting large amounts of gases (e.g., oxygen (O_2) and carbon dioxide (CO_2)) and compounds (e.g., acids, bases, and salts), resulting in enhanced silicate weathering^{37,38,48}. Thus, silicate weathering in mid-latitude regions may also respond sensitively to rainfall variability, and these results further support previous studies that identified rainfall as the primary control of silicate weathering in mid-latitude regions^{37,38}.

Some modern observational studies have shown that rainfall not only increases weathering intensity by supplying fluid for chemical reactions⁴⁸ but also weakens it by driving erosion, such as storm-triggered mass wasting, thereby decreasing the soil residence time available for chemical reactions^{41,49}. Therefore, these observations suggest that there is no obvious linear relationship between rainfall and weathering intensity. However, erosion occurs mainly in limited areas and for short periods. The weathered products observed in the marginal sea are transported over long periods by large rivers before finally being deposited, and large rivers generally have large-scale areas of alluvial plains and sedimentary basins, which provide sufficient time for chemical reactions to occur in detrital material produced by physical denudation. Accordingly, increased rainfall generally enhances chemical weathering in large river basins.

Overall, silicate weathering in the mid-latitude regions responded sensitively to both temperature and rainfall variability on orbital timescales. Here, the temperature variability in mid- to high-latitude regions was in phase with the dynamics of high-latitude ice sheets, whereas the rainfall variability was mainly modulated by low-latitude monsoon systems⁹. As a result, the multiple evolution periods of the weathering records at Site LV55-38-3 indicate that the weathering process in mid-latitude regions was modulated jointly by both high-latitude ice sheets and low-latitude monsoons. Moreover, the $\delta^{13}\text{C}$ record of loess carbonates from mid-latitude Chinese Loess Plateau (Jing Yuan, 36°20'N, 104°37'E, 2210 m above sea level) also has a relatively strong power of combined 100-, 41-, and 23-kyr cycles during the late Quaternary^{50,51} (Figs. 3f and S12). The $\delta^{13}\text{C}$ values of loess carbonates mainly reflect terrestrial vegetation changes and are also closely related to temperature and rainfall variability, similar to the silicate weathering process. In this record, the $\delta^{13}\text{C}$ values were low during interglacials and high during glacials (Fig. 3f), clearly following the variation in SST at middle and high latitudes. Similarly, in the precession band, lower $\delta^{13}\text{C}$ values correspond to increased rainfall periods (Fig. S15), paralleling the weathering records in the Sea of Okhotsk. Therefore, loess $\delta^{13}\text{C}$ records also reflect the combined influence of high-latitude ice sheets and low-

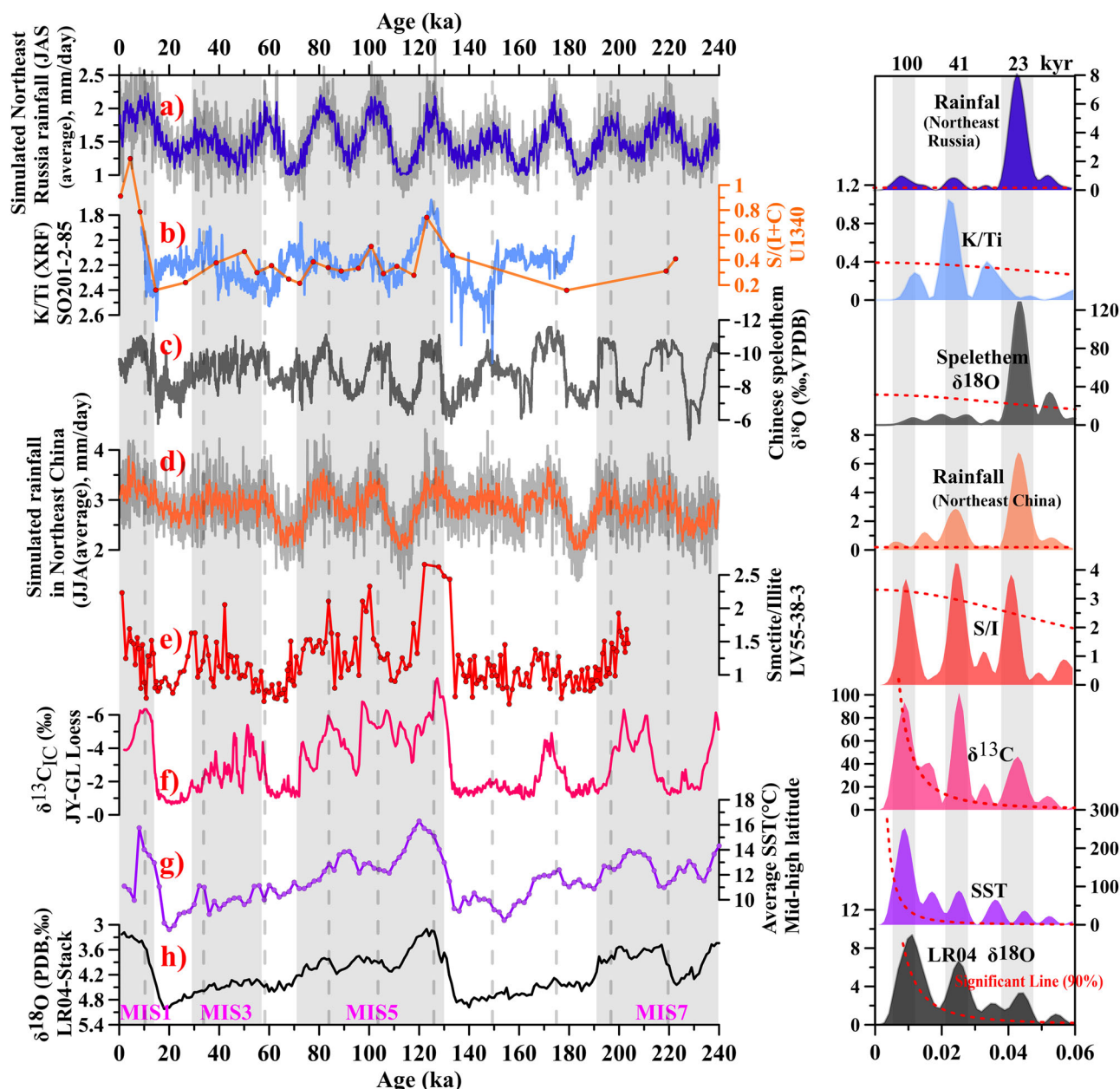


Fig. 3 | Comparison of weathering records in mid-to high-latitude regions with mid-to high-latitude temperatures, nearby simulated rainfall records, and paleoenvironment records from the Chinese Loess Plateau (CLP), as well as their corresponding spectral analysis results (right). a Simulated rainfall (July–August–September (JAS) average) in Northeast Russia (sediment source of the Bering Sea), **(b)** K/Ti ratios (XRF) from Site SO201-2-85KL³⁰ and smectite/ (illite + chlorite) ratios from Site U1340⁵³, **(c)** Chinese speleothem $\delta^{18}\text{O}$ record from

Sanbao, Hulu and Dongge caves⁸, **(d)** Simulated rainfall (June–July–August (JJA) average) in Northeast China (sediment source of the Sea of Okhotsk), **(e)** Smectite/illite ratios of Site LV55-38-3 (this study), **(f)** $\delta^{13}\text{C}$ values of loess carbonate⁵⁰, **(g)** Averaged sea surface temperature (SST) in mid- to high-latitude regions^{42–45}, **(h)** 57 stacked, globally distributed benthic $\delta^{18}\text{O}$ records (LR04 Stack)⁴. Notes: In the spectral analysis, the red dotted lines indicate the 90% significance level.

latitude monsoon systems on climate variations in the middle latitudes (East Asian monsoon region).

High-latitude regions. Similar to observations in the Sea of Okhotsk, the K/Ti weathering proxies from two sites (SO201-2-85KL and SO201-2-101KL) in the high-latitude Bering Sea exhibit distinct glacial-interglacial cycles³⁰ (Fig. 3b). These variations closely track the SST pattern observed in mid-to high-latitude regions of the NH (Fig. 3g), showing reduced K/Ti ratios during interglacial periods and elevated ratios during glacial intervals. Both study sites, located in the western Bering Sea, receive sediments primarily from the adjacent Northeast Russian continental margin (Supplementary Text S2), suggesting that temperature variability

exerts a dominant control on silicate weathering in this high-latitude region of Northeast Russia. For rainfall variability, simulated rainfall records from high-latitude Northeast Russia display significant 23-kyr cycles (Fig. 3a), analogous to those observed in mid-latitude Northeast China. However, the 23-kyr cycles are weak in the weathering records of the Bering Sea. Hence, the influence of rainfall variability on silicate weathering is negligible in high-latitude regions. Compared with Northeast China, Northeast Russia is closer to ice sheets, and the dynamics of ice sheets could drive significant temperature fluctuations during glacial-interglacial periods, ultimately impacting silicate weathering processes in this region⁵². Collectively, the evident glacial-interglacial cycles of the weathering records in the Bering Sea indicate

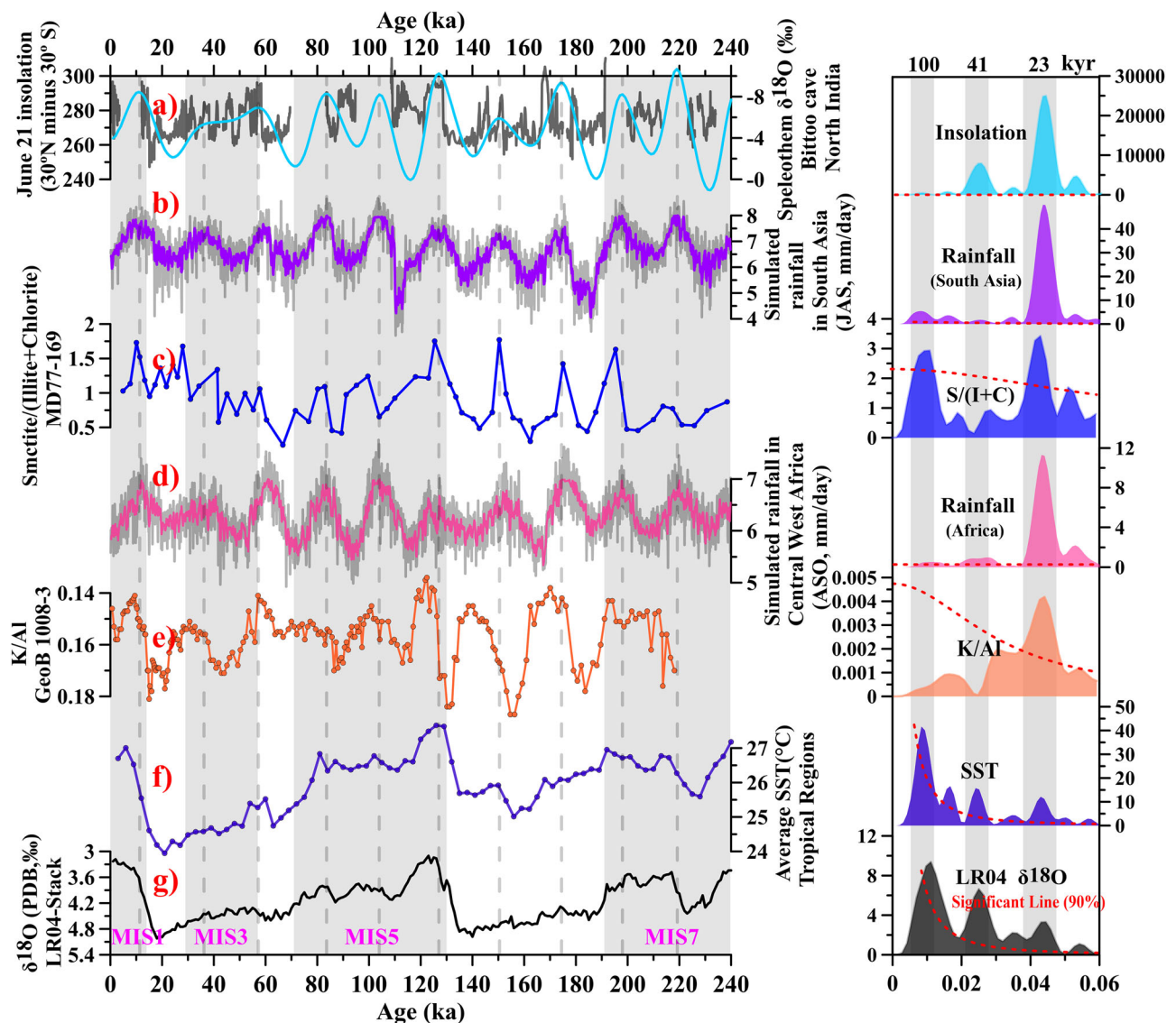


Fig. 4 | Comparison of weathering records in tropical regions (Central West Africa and South Asia) with tropical temperature and nearby simulated rainfall records, as well as their corresponding spectral analysis results (right). a Indian summer rainfall record reconstructed from the Bittoe Cave speleothem (black line)⁶² and June 21 insolation differential between 30°N and 30°S (sky blue line)¹⁰. **b** Simulated rainfall (July–August–September (JAS) average) in South Asia

(sediment source of the Bay of Bengal), **(c)** Smectite/(illite + chlorite) ratios from Site MD77-169³², **(d)** Simulated rainfall (August–September–October (ASO) average) in Central West Africa (sediment source of the Gulf of Guinea), **(e)** K/Al ratios from Site GeoB1008-3³⁴, **(f)** Average sea surface temperature (SST) in tropical regions^{63,64}, **(g)** 57 stacked, globally distributed benthic $\delta^{18}\text{O}$ records (LR04 stack)⁴. Note: In the spectral analysis, the red dotted lines indicate the 90% significance level.

that silicate weathering at high latitudes was primarily influenced by high-latitude ice sheets.

The low-resolution smectite/(illite + chlorite) record at Site U1340 (53°24'N, 179°31'W; water depth: 1295 m, Fig. S12) in the Bering Sea also shows distinct glacial-interglacial cycles, with high values during interglacials and low values during glacials⁵³ (Fig. 3b). In the Bering Sea, smectite mainly originates from the rapid chemical weathering of basic volcanic rocks in the Aleutian Island arc, whereas illite and chlorite are mainly formed by the physical weathering of rocks from the surrounding continents^{53,54}. Therefore, the smectite/(illite + chlorite) ratio at Site U1340 serves as a reliable proxy for silicate weathering intensity in the continental regions surrounding the Bering Sea⁵³. The strong covariation between the smectite/(illite + chlorite) ratios and mid-to-high-latitude SST records implies that silicate weathering in high-latitude regions is mechanistically linked to ice sheet dynamics.

Low-latitude regions. At low latitudes, it is evident that the weathering proxies in the Gulf of Guinea near Central West Africa and the Bay of

Bengal near South Asia display notable 23-kyr cycles (Supplementary Text S2 and Fig. 4c, e). The two Gulf of Guinea sites GeoB4901-8 and GeoB1008-3 are located in the estuaries of the Niger River and Congo River, respectively^{33,34}, and receive substantial amounts of sediment from the Niger River and Congo River Basins under the influence of the African monsoons. Many records (e.g., dust flux⁵⁵, lake level⁵⁶, and freshwater discharge⁵⁷) show that African monsoon rainfall is controlled by the north-south displacement of the Intertropical Convergence Zone (ITCZ) under the influence of low-latitude solar radiation, which dominantly exhibits precession (23-kyr) cycles^{13,55,58,59} (Fig. S17). Similarly, the simulated rainfall over Central West Africa exhibits pronounced 23-kyr cycles. Cross-spectral and wavelet analyses reveal that in the precession band, weathering proxies correlate well with simulated rainfall (Figs. S18 and S19), where increased rainfall coincides with enhanced silicate weathering. Therefore, silicate weathering in the Gulf of Guinea region is closely related to rainfall variability. Furthermore, modern observations show that increased rainfall always leads to high output of kaolinite, a

product of intense weathering, in the rivers in Central West Africa. This finding reinforces the notion that weathering processes are highly sensitive to monsoon rainfall in low-latitude Africa^{60,61}.

In addition, three sites (U1425, MD77-169, and MD77-171) in the Bay of Bengal receive considerable sediment from South Asia under the influence of Indian summer monsoon rainfall^{31,32}. Similar to records in Central West Africa, the simulated and reconstructed (i.e., speleothem $\delta^{18}\text{O}$) rainfall records in South Asia exhibit strong 23-kyr cycles during the late Quaternary (Fig. 4a, b). In the precession band, the smectite/(illite + chlorite) ratio correlates closely with oxygen isotopic compositions from Bittoo Cave and with simulated rainfall records in South Asia, the main sediment source for the Bay of Bengal⁶² (Fig. 4a–c). As rainfall intensifies (reflected by decreased speleothem $\delta^{18}\text{O}$ values and elevated simulated rainfall), the smectite/(illite + chlorite) ratio increases, indicating enhanced silicate weathering in the South Asia sediment source region^{20,31,32}. This covariation is further supported by cross-spectral and wavelet analyses, which reveal coherent periodicities between weathering records and simulated rainfall at 23-kyr cycles (Figs. S19 and S20). Consequently, silicate weathering in South Asia is highly sensitive to rainfall variability in the precession band.

The influence of temperature on silicate weathering also requires consideration. Similar to the SST at middle and high latitudes, the compiled average SST in tropical regions also displays distinct glacial-interglacial cycles (dominated by 100-kyr cycles; Figs. 4f and S21). However, weathering proxies in the Gulf of Guinea do not have significant correlations with tropical SST in the 100-kyr band (Fig. S18). SST variability in low-latitude areas is only 2–3 °C over glacial-interglacial cycles^{63,64} (Fig. S21), which is substantially lower than that in mid- and high-latitude areas (8–12 °C). Therefore, low SST variability may lead to the negligible influence of temperature on silicate weathering in low-latitude Central West Africa. Considering the presence of 100-kyr cycles in the K/Al ratio observed at Site GeoB4901-8, we speculate that other factors, such as sea level and ocean currents, may exert potential influences.

Whereas the weathering records (smectite/(illite + chlorite)) in the Bay of Bengal have obvious glacial-interglacial cycles, and there are strong correlations between the smectite/(illite + chlorite) ratios (Sites U1445 and MD77-169) and tropical SST over the 100-kyr band (Fig. S20). As shown in Fig. 4c, f, elevated SST during interglacial periods correspond to increased smectite/(illite + chlorite) ratios, whereas glacial intervals characterized by decreased SST exhibit significantly lower smectite/(illite + chlorite) ratios. Provenance analyses confirm that Bay of Bengal sediments are derived primarily from high-elevation Himalayan regions^{20,31,32}. According to modern observations, because of the increasing diabatic processes in the middle and high troposphere resulting from cloud condensation, there are greater temperature fluctuations in high-elevation regions than in low-elevation regions^{65,66}. Consequently, although located in low-latitude regions, these high-elevation Himalayan terrains experienced substantial temperature variability during glacial-interglacial cycles. This implies that temperature also exerts a significant influence on silicate weathering in South Asia. However, compared with those in the mid- and high-latitude regions, the Bay of Bengal weathering proxies show more pronounced 23-kyr fluctuations and stronger correlations with rainfall variability in the precessional band (Fig. 4b, c). These findings suggest that rainfall plays a more important role in regulating silicate weathering in South Asia than temperature does.

In summary, silicate weathering records in low-latitude regions show clear 23-kyr cycles and are more sensitive to rainfall variability than to temperature fluctuations. At low latitudes, rainfall is the main characteristic of low-latitude monsoons and is regulated by tropical solar radiation⁹. These observations establish monsoon rainfall as the dominant control of orbital-scale silicate weathering in low-latitude regions. In contrast, the distinct 100-kyr cycles in the Bay of Bengal weathering record are primarily linked to high-elevation sediment sources in South Asia. High-elevation regions exhibit considerable temperature variability during glacial-interglacial cycles, which may have a significant influence on weathering processes across this region. Here, temperature records from both the NH and Southern Hemisphere (SH) show patterns that are broadly similar to the

records of ice volume and Antarctic temperature, which are modulated by high-latitude ice sheets⁹. Therefore, clear 100-kyr cycles in the low-latitude weathering records imply that silicate weathering was also regulated by high-latitude ice sheets, but this influence seems to be mainly limited to high-elevation areas. This pattern is confirmed by the lacustrine record from Lake Junín (11°S, 76°W, 4100 m above sea level, Fig. S12) in the uppermost Amazon basin⁶⁷. Lithogenic proxies sensitive to tropical glaciation in Lake Junín show clear 100-kyr cycles over the last 700 ka, indicating that the ice sheets influence tropical Andean glaciers through interhemispheric climatic teleconnections⁶⁷.

Implications

In conclusion, there are obvious differences in the response of silicate weathering to temperature and rainfall variability at different latitudes. In mid-latitude regions (Sea of Okhotsk), silicate weathering (with strong 100-, 41- and 23-kyr cycles) shows heightened sensitivity to both temperature and rainfall variability, reflecting the combined impact of high-latitude ice sheets and low-latitude monsoon rainfall on this process. Conversely, in high-latitude regions, silicate weathering (with strong 100-kyr cycles) responds more strongly to temperature fluctuations, demonstrating predominant high-latitude ice sheets influence. In tropical regions, silicate weathering (with strong 23-kyr cycles) is more responsive to rainfall variability, highlighting primary modulation by low-latitude monsoons.

Therefore, the heterogeneous responses of silicate weathering to temperature and rainfall variations indicate that neither low-latitude monsoon systems nor high-latitude ice sheet dynamics alone can fully explain weathering rate fluctuations on orbital timescales. A synergistic interplay between these two mechanisms appears necessary to provide a more robust and comprehensive interpretation of the observed weathering patterns. Cheng et al.⁹ recently proposed a new orbital hypothesis related to climate change that seeks to expand upon the classical Milankovitch theory. According to their hypothesis, the dominant factor in global climate change on the orbital timescale should not be limited to ice sheets driven by high-latitude summer solar radiation. Instead, low-latitude monsoon variability, driven by tropical summer insolation (i.e., the Kutzbach orbital–monsoon hypothesis), also plays a crucial role in the climate system. This new framework incorporates changes in ice sheets due to high-latitude solar radiation and their global effects (e.g., temperature variations), alongside alterations in the global monsoon system (particularly the low-latitude hydrological cycle) resulting from solar insolation differences at low latitudes (~30°N to ~30°S). This comprehensive approach offers a more complete understanding of the evolution of global climate systems. Here, silicate weathering was shown to respond more sensitively to rainfall variability in low-latitude regions, to temperature variability in high-latitude regions, and to both temperature and rainfall in mid-latitude regions, which corresponds well to the “Milankovitch–Kutzbach” hypothesis, suggesting that high-latitude ice sheets and low-latitude monsoons may jointly control global-scale climate change. Collectively, our findings advance the understanding of the mechanism of climate change on orbital timescales, providing key insights into Earth’s surface climate evolution.

Nevertheless, relying solely on silicate weathering records from disparate latitudinal regions to investigate orbital-scale variations and their linkages with temperature/rainfall—and by extension, the governing mechanisms of the climate system—remains insufficient. Future studies should integrate broader geological proxies and advanced statistics to achieve a more holistic understanding of Earth’s climate system evolution on orbital timescales.

Materials and methods

Materials and age model

The sediment core LV55-38-3 (48°40'N, 146°57'E) was collected off the southeastern Sakhalin Island in the western Sea of Okhotsk at a water depth of 1026 m (Fig. S1), and retrieved using a gravity corer aboard R/V Akademik Lavrentiev during the 2011 joint Chinese-Russian expeditions (Cruise LV55). The sediments in core LV55-38-3 are mainly composed of

silty sand and silty clay with dispersed gravel. The core was subsampled at 2 cm intervals. Additionally, 30 surface sediment samples from cruises LV55 and LV87 in the Sea of Okhotsk were selected for sediment provenance analysis (Fig. S1).

The LV55-38-3 age model was established based on a combination of radiocarbon dating (AMS^{14}C) and high-resolution X-ray fluorescence (XRF) data correlated with the global composite benthic foraminiferal oxygen isotope curves⁴ (LR04 stack; detailed information on AMS^{14}C dating and XRF analysis is provided in Supplementary Text S3 and Table S1).

High-resolution XRF records of $\log(\text{Si}/\text{Al})$, Ba/Al ratios, as well as element Al counts and Ti counts from LV55-38-3, show coherent patterns with clear glacial-interglacial cycles (Fig. S22). XRF data were validated by lower-resolution ICP-OES/MS measurements (Fig. S22). In the subarctic Pacific and its marginal sea, Ba and Si track surface productivity^{30,68,69}, whereas elevated Al and Ti indicate increased terrigenous input⁷⁰. As previously discussed, subarctic Pacific export productivity covaries with the global climate, with higher values during interglacial periods and lower values during glacial intervals^{30,68,69}. Fluctuations in sea level also modulated the input of terrigenous sediments, with greater input during glacial periods when the sea level was low⁷⁰. As a result, both productivity (e.g., Ba/Al and Si/Al ratios) and detrital (e.g., Al and Ti counts) proxies in core LV55-38-3 show clear glacial-interglacial variations and could be correlated with the LR04 stack (Fig. S22). Age-depth data are provided in the Table S2.

To validate the chronological data of Site LV55-38-3, we carried out a comparative analysis of the total organic matter (TOC) and total nitrogen (TN) contents based on the newly established age model with the LR04 stack and the TOC contents from Sites MR0604-PC-7R and MD01-2415 in the Sea of Okhotsk, both of which have credible age-depth models (Fig. S1)^{71,72}. In the Subarctic Pacific, TOC and TN are closely correlated with biological productivity and can be correlated with the LR04 stack⁷³. As shown in Fig. S23, both TOC and TN contents at Site LV55-38-3 reveal clear glacial-interglacial cycles, which are in excellent agreement with the TOC records from sites MR0604-PC-7R and MD01-2415. This consistency validates the LV55-38-3 chronology.

Clay minerals

Sediment samples were first treated with acetic acid (15%) and hydrogen peroxide (30%) to remove carbonate and organic matter, respectively. The residual detritus was used for clay-sized separation. Particles $<2\ \mu\text{m}$ were separated according to Stoke's settling velocity principle²⁰. The extracted clay fractions were smeared onto glass slides and dried at room temperature. Clay mineral analysis was conducted by X-ray diffraction (XRD) using a D8 ADVANCE diffractometer with $\text{CuK}\alpha$ (alpha) radiation (40 kV, 40 mA) at the Institute of Oceanology, Chinese Academy of Sciences (IOCAS)⁷⁴. The peak areas of the basal reflections for the main clay mineral groups (smectite-17 Å, illite-10 Å, and kaolinite/chlorite-7 Å) were estimated based on diffractograms of ethylene-glycolate samples using Topas 2 P software. Relative abundances were calculated through peak area multiplication with empirical factors⁷⁵. The relative error was less than 5% for the replicate analysis of selected samples. A total of 187 samples from core LV55-38-3 were used for clay mineral analyses.

Major and trace element analysis

A total of 96 samples from core LV55-38-3 and 30 surface sediment samples were subjected to major and trace element analyses ($<2\ \mu\text{m}$). The $<2\ \mu\text{m}$ siliciclastic sediments for major and trace element analyses were extracted using the same procedures as those used for clay mineral analysis²⁰. The samples were dried and ground to less than 200 mesh, and approximately 50.00 mg of powder sample was weighed into Teflon containers. A mixture of double-distilled HF and HNO_3 (1:1) was subsequently added to completely digest the samples (at 190 °C for 48 h). The samples were then dried and placed in a known volume of 2% HNO_3 . Major and trace element content was measured using ICP-OES and ICP-MS, respectively. These measurements were conducted at the Key Laboratory of Marine Geology and Metallogeny, First Institute of Oceanography, Ministry of Natural

Resources. The national reference material, GWB07309 (GSD-9), a blank sample, and replicate samples were used to monitor the analytical process. The repeated measurements and GSD-9 standard sample analysis results revealed that the relative standard deviation of major elements was less than 3%, and the error for trace elements and rare earth elements was less than 6%. To verify the reliability of elements Al, Ti, and Ba measurements obtained by XRF, we also analyzed low-resolution major and trace elements in 95 bulk sediment samples from Site LV55-38-3 using ICP-OES and ICP-MS, using methods similar to those applied to clay-sized sediments.

Compilation of existing silicate weathering records

Silicate weathering data from various geographical regions were compiled, including two high-latitude sites in the Bering Sea (Sites SO201-2-85KL (57°30'N, 170°24'E, water depth: 968 m) and SO201-2-101KL (58°52'N, 170°41'E, water depth: 630 m)) and five low-latitude sites (Fig. 1). Sites GeoB4901-8 (02°40'N, 06°43'E, water depth: 2184 m) and GeoB1008-3 (06°35'S, 10°19'E, water depth: 3124 m) are located in the Gulf of Guinea near Central West Africa^{33,34}, while Sites U1445 (17°44'N, 84°47'E, water depth: 2513 m), MD77-169 (10°12'N, 95°03'E, water depth: 2360 m), and MD77-171 (11°45'N, 94°09'E, water depth: 1760) are located in the Bay of Bengal near South Asia^{20,31,32}. Common weathering proxies, such as the K/Al ratio, K/Ti ratio, and smectite/(illite + chlorite) ratio, were chosen to reflect the intensity of chemical weathering in the sediment source regions. A detailed description is provided in Supplementary Text S2. The cores from these sites have age spans exceeding 150 ka and temporal resolutions generally better than 4 kyr. The age models used for these sites are reliable, even with different dating techniques. More information on the adoption of weathering proxies and the age model for each site can be found in Table S3.

Climate model and simulation

The fully-coupled NCAR-CCSM3 model was employed in this work to simulate the evolution of the global climate over the last 300 ka. This model has a spatial resolution of $\sim 3.75^\circ$ for the atmosphere (26 vertical layers) and land. The latitudinal resolution varies, with a finer resolution of approximately 0.9° near the equator and coarser resolutions toward the poles. The ocean and sea ice data have a longitudinal resolution of approximately 3.6° , with 25 vertical layers^{76–79}.

To compare the reconstructed rainfall variability across different latitudes, we analyzed a transient simulation driven by realistic transient forcings of orbital parameters, greenhouse gases, and continental ice sheets over the last 240 ka (referred to as ORB + GHG + ICE⁷⁶). Note that, to save the computational burden, the orbital parameters and greenhouse gas concentrations were accelerated by a factor of 100, meaning that 1 model year in the simulation represents 100 years of climate evolution in real-time. The continental ice sheet was updated based on the ICE-5G (VM2) reconstruction⁷⁷. The response of the surface climate to external forcings is generally fast and not affected by acceleration in terms of its phase. More details of the model setup can be found in Lu et al.⁷⁶.

Time series analysis

To elucidate the orbital-scale evolution of weathering records across different latitudes and its link to temperature and rainfall during the late Quaternary, time series analysis was performed, including spectral analysis, cross-spectral analysis, and cross-wavelet analysis. Spectral analysis was first performed on the original silicate weathering records, compiled SST, and simulated rainfall records. All datasets were then linearly interpolated to a 1-kyr resolution to enable cross-spectral and wavelet analyses.

Spectral analysis was performed using PAST software with a rectangular window function⁸⁰. The 90% significance levels against red noise are indicated in the power spectra. To elucidate the linkage between silicate weathering and rainfall/temperature variations on orbital timescales, we conducted cross-spectral and wavelet analyses. Cross-spectral analysis was implemented using the ARAND software package⁸¹, with results displayed as normalized spectral density (variance/frequency, log-scaled) and coherence (0–0.06 frequency band). Coherency measures the maximum linear

correlation between phase-aligned signals (0–1), with significance thresholds at 80% and 95% confidence levels. Cross-wavelet analysis was performed using Acycle software⁸², and the related calculations and descriptions can be found in the previous publications⁸³. In the cross-wavelet analysis, arrows pointing to the right indicate an in-phase relationship, suggesting a positive correlation. The arrows pointing to the left represent an antiphase relationship, indicating a negative correlation.

Data availability

All proxy and simulation data are available online for download at Zenodo (<https://doi.org/10.5281/zenodo.15471976>).

Received: 21 January 2025; Accepted: 5 May 2025;

Published online: 23 May 2025

References

- Milankovitch, M. *Canon of Insolation and the Iceage Problem* (Royal Serbian Academy Special Publication, 1941). (in German).
- Hays, J. D., Imbrie, J. & Shackleton, N. J. Variations in the Earth's orbit: pacemaker of the ice ages. *Science* **194**, 1121 (1976).
- Imbrie, J. et al. The orbital theory of Pleistocene climate: support from a revised chronology of the marine $\delta^{18}\text{O}$ record. in *Milankovitch and Climate Part I* (eds Berger, A. L., Imbrie, J., Hays, J., et al.) 269–305 (D. Reidel Publishing Company, Netherlands, 1984).
- Lisiecki, L. E. & Raymo, M. E. A Pliocene-Pleistocene stack of 57 globally distributed benthic $\delta^{18}\text{O}$ records. *Paleoceanography* **20**, 1–17 (2005).
- EPICA C. Members Eight glacial cycles from an Antarctic ice core. *Nature* **429**, 623–628 (2004).
- Liu, T. & Ding, Z. Chinese loess and the paleomonsoon. *Annu. Rev. Earth Planet. Sci.* **26**, 111–145 (1998).
- An, Z. et al. Glacial-interglacial Indian summer monsoon dynamics. *Science* **333**, 719–723 (2011).
- Cheng, H. et al. The Asian monsoon over the past 640,000 years and ice age terminations. *Nature* **534**, 640–646 (2016).
- Cheng, H. et al. Milankovitch theory and monsoon. *Innovation* **3**, 100338 (2022).
- Laskar, J. et al. Long term evolution and chaotic diffusion of the insolation quantities of Mars. *Icarus* **170**, 343–364 (2004).
- Tachikawa, K. et al. The precession phase of hydrological variability in the Western Pacific Warm Pool during the past 400 ka. *Quat. Sci. Rev.* **30**, 3716–3727 (2011).
- Beck, J. W. et al. A 550,000-year record of East Asian monsoon rainfall from 10Be in loess. *Science* **360**, 877 (2018).
- Bastian, L. et al. Co-variations of climate and silicate weathering in the Nile Basin during the Late Pleistocene. *Quat. Sci. Rev.* **264**, 107012 (2021).
- Yang, C., Vigier, N., Yang, S., Revel, M. & Bi, L. Clay Li and Nd isotopes response to hydroclimate changes in the Changjiang (Yangtze) basin over the past 14,000 years. *Earth Planet. Sci. Lett.* **561**, 116793 (2021).
- Li, C. & Yang, S. Is chemical index of alteration (CIA) a reliable proxy for chemical weathering in global drainage basins?. *Am. J. Sci.* **310**, 111–127 (2010).
- Qiu, S. et al. Chemical weathering of monsoonal eastern China: implications from major elements of topsoil. *J. Asian Earth Sci.* **81**, 77–90 (2014).
- Yang, Y. et al. Monsoon-enhanced silicate weathering as a new atmospheric CO₂ consumption mechanism contributing to fast late miocene global cooling. *Paleoceanogr. Paleoclimatol.* **36**, 1–26 (2021).
- Nesbitt, H. W., Markovics, G. & price, R. C. Chemical processes affecting alkalis and alkaline earths during continental weathering. *Geochim. Cosmochim. Acta* **44**, 1659–1666 (1980).
- Wan, S. et al. Tectonic and climatic controls on long-term silicate weathering in Asia since 5 Ma. *Geophys. Res. Lett.* **39**, 1–5 (2012).
- Yu, Z., Colin, C., Bassinot, F., Wan, S. & Bayon, G. Climate-driven weathering shifts between highlands and floodplains. *Geochim. Geophys. Geosyst.* **21**, 1–16 (2020).
- Dosseto, A. et al. Rapid response of silicate weathering rates to climate change in the Himalaya. *Geochem. Perspect. Lett.* **1**, 10–19 (2015).
- Xu, F. et al. Provenance and weathering of sediments in the deep basin of the northern South China Sea during the last 38 kyr. *Mar. Geol.* **440**, 106602 (2021).
- Shakun, J. D., Lea, D. W., Lisiecki, L. E. & Raymo, M. E. An 800-kyr record of global surface ocean $\delta^{18}\text{O}$ and implications for ice volume-temperature coupling. *Earth Planet. Sci. Lett.* **426**, 58–68 (2014).
- Wang, P. X. et al. The global monsoon across time scales: mechanisms and outstanding issues. *Earth Sci. Rev.* **174**, 84–121 (2017).
- Wan, S. et al. Enhanced silicate weathering of tropical shelf sediments exposed during glacial lowstands: a sink for atmospheric CO₂. *Geochim. Cosmochim. Acta* **200**, 123–144 (2017).
- Hu, D. et al. Deep sea records of the continental weathering and erosion response to East Asian monsoon intensification since 14ka in the South China Sea. *Chem. Geol.* **326–327**, 1–18 (2012).
- Clift, P. D., Wan, S. & Blusztajn, J. Reconstructing chemical weathering, physical erosion and monsoon intensity since 25Ma in the northern South China Sea: a review of competing proxies. *Earth Sci. Rev.* **130**, 86–102 (2014).
- Selvaraj, K. & Chen, C.-T. A. Moderate chemical weathering of subtropical Taiwan: constraints from solid-phase geochemistry of sediments and sedimentary rocks. *J. Geol.* **114**, 101–116 (2006).
- Dinis, P. A., Garzanti, E., Hahn, A., Vermeesch, P. & Cabral-Pinto, M. M. S. Weathering indices as climate proxies. A step forward based on Congo and SW African river muds. *Earth Sci. Rev.* **201**, 103039 (2020).
- Riethdorf, J. R. et al. Millennial-scale variability of marine productivity and terrigenous matter supply in the western Bering Sea over the past 180 kyr. *Clim. Past* **9**, 1345–1373 (2013).
- Lee, J. et al. Indian monsoon variability in the Mahanadi Basin over the last two glacial cycles and its implications on the Indonesian throughflow. *Geosci. Front.* **14**, 101483 (2022).
- Colin, C., Turpin, L., Bertaux, J., Desprairies, A. & Kissel, C. Erosional history of the Himalayan and Burman ranges during the last two glacial-interglacial cycles. *Earth Planet. Sci. Lett.* **171**, 647–660 (1999).
- Zabel, M. et al. Late quaternary climate changes in Central Africa as inferred from terrigenous input to the Niger Fan. *Quat. Res.* **56**, 207–217 (2001).
- Schneider, R. R., Price, B., Müller, P. J., Kroon, D. & Alexander, I. Monsoon related variations in Zaire (Congo) sediment load and influence of fluvial silicate supply on marine productivity in the east equatorial Atlantic during the last 200,000 years. *Paleoceanography* **12**, 463–481 (1997).
- Börker, J. et al. Chemical weathering of loess and its contribution to global alkalinity fluxes to the coastal zone during the last glacial maximum, mid-Holocene, and present. *Geochem. Geophys. Geosyst.* **21**, e2020GC008922 (2020).
- Hartmann, J. et al. Global CO₂-consumption by chemical weathering: WHAT is the contribution of highly active weathering regions?. *Glob. Planet. Change* **69**, 185–194 (2009).
- Hartmann, J. & Moosdorf, N. Chemical weathering rates of silicate-dominated lithological classes and associated liberation rates of phosphorus on the Japanese Archipelago—implications for global scale analysis. *Chem. Geol.* **287**, 125–157 (2011).
- Moosdorf, N., Hartmann, J., Lauerwald, R., Hagedorn, B. & Kempe, S. Atmospheric CO₂ consumption by chemical weathering in North America. *Geochim. Cosmochim. Acta* **75**, 7829–7854 (2011).
- Wang, B., Liu, J., Kim, H.-J., Webster, P. J. & Yim, S.-Y. Recent change of the global monsoon precipitation (1979–2008). *Clim. Dyn.* **39**, 1123–1135 (2011).
- Dessert, C., Gaillardet, J., Dupre, B., Schott, J. & Pokrovsky, O. S. Fluxes of high- versus low-temperature water–rock interactions in

- aerial volcanic areas: example from the Kamchatka Peninsula, Russia. *Geochim. Cosmochim. Acta* **73**, 148–169 (2009).
41. Deng, K., Yang, S. & Guo, Y. A global temperature control of silicate weathering intensity. *Nat. Commun.* **13**, 1781 (2022).
42. Herbert, T. et al. Collapse of the California Current during glacial maxima linked to climate change on land. *Science* **293**, 71–76 (2001).
43. Lattaud, J. et al. A multiproxy study of past environmental changes in the Sea of Okhotsk during the last 1.5 Ma. *Org. Geochem.* **132**, 50–61 (2019).
44. Ruddiman, W. F., Raymo, M. E., Martinson, D. G., Clement, B. M. & Backman, J. Pleistocene evolution: Northern hemisphere ice sheets and North Atlantic Ocean. *Paleoceanogr. Paleoclimatol.* **4**, 353–412 (1989).
45. Naafs, B. D. A. et al. Strengthening of North American dust sources during the late Pliocene (2.7 Ma). *Earth Planet. Sci. Lett.* **317**, 8–19 (2012).
46. Huang, E. et al. Dole effect as a measurement of the low-latitude hydrological cycle over the past 800 ka. *Sci. Adv.* **6**, eaba4823 (2020).
47. Guo, B. et al. Dominant precessional forcing of the East Asian summer monsoon since 260 ka. *Geology* **50**, 1372–1376 (2022).
48. Maher, K. & Chamberlain, C. P. Hydrologic regulation of chemical weathering and the geologic carbon cycle. *Science* **343**, 1502–1504 (2014).
49. Ferrier, K. L., Huppert, K. L. & Perron, J. T. Climatic control of bedrock river incision. *Nature* **496**, 206–209 (2013).
50. Sun, Y. et al. Astronomical and glacial forcing of East Asian summer monsoon variability. *Quat. Sci. Rev.* **115**, 132–142 (2015).
51. Sun, Y. et al. Diverse manifestations of the mid-Pleistocene climate transition. *Nat. Commun.* **10**, 352 (2019).
52. Miller, G. H. et al. Arctic amplification: can the past constrain the future?. *Quat. Sci. Rev.* **29**, 1779–1790 (2010).
53. Zhang, Q. et al. Clay mineral assemblages at IODP Site U1340 in the Bering Sea and their paleoclimatic significance. *Sci. China Earth Sci.* **58**, 707–717 (2015).
54. Naidu, A. S., Han, M. W., Mowatt, T. C. & Wajda, W. Clay minerals as indicators of sources of terrigenous sediments, their transportation and deposition: Bering Basin, Russian-Alaskan Arctic. *Mar. Geol.* **127**, 87–104 (1995).
55. Skonieczny, C. et al. Monsoon-driven Saharan dust variability over the past 240,000 years. *Sci. Adv.* **5**, 1–8 (2019).
56. deMenocal, P. B., Ruddiman, W. F. & Pokras, E. M. Influences of high- and low-latitude processes on African terrestrial climate: Pleistocene eolian records from equatorial Atlantic ocean drilling program site 663. *Paleoceanography* **8**, 209–242 (1993).
57. Tierney, J. E., deMenocal, P. B. & Zander, P. D. A climatic context for the out-of-Africa migration. *Geology* **45**, 1023–1026 (2017).
58. Tierney, J. E., Pausata, F. S. R. & deMenocal, P. B. Rainfall regimes of the Green Sahara. *Sci. Adv.* **3**, e1601503 (2017).
59. Newton, A., Thunell, R. & Stott, L. Climate and hydrographic variability in the Indo-Pacific Warm Pool during the last millennium. *Geophys. Res. Lett.* **33**, 1–5 (2006).
60. Pastouret, L., Chamley, H., Delibrias, G., Duplessy, J. & Thiede, J. Late Quaternary climatic changes in western tropical Africa deduced from deep-sea sedimentation off the Niger delta. *Oceanol. Acta* **1**, 217–232 (1978).
61. Bonifay, D. & Giresse, P. Middle to late Quaternary sediment flux and post-depositional processes between the continental slope off Gabon and the Mid-Guinean margin. *Mar. Geol.* **106**, 107–129 (1992).
62. Kathayat, G. et al. Indian monsoon variability on millennial-orbital timescales. *Sci. Rep.* **6**, 24374 (2016).
63. Herbert, T. D., Peterson, L. C., Lawrence, K. T. & Liu, Z. Tropical ocean temperatures over the past 3.5 million years. *Science* **328**, 1530–1534 (2010).
64. Liu, Z. & Herbert, T. D. High-latitude influence on the eastern equatorial Pacific climate in the early Pleistocene epoch. *Nature* **427**, 720–723 (2004).
65. Dong, D., Huang, G., Qu, X., Tao, W. & Fan, G. Temperature trend–altitude relationship in China during 1963–2012. *Theor. Appl. Climatol.* **122**, 285–294 (2015).
66. Ohmura, A. Enhanced temperature variability in high-altitude climate change. *Theor. Appl. Climatol.* **110**, 499–508 (2012).
67. Rodbell, D. et al. 700,000 years of tropical Andean glaciation. *Nature* **607**, 301–306 (2022).
68. Jaccard, S. L. et al. Glacial/interglacial changes in Subarctic North Pacific stratification. *Science* **308**, 1003–1006 (2005).
69. Jaccard, S. L., Galbraith, E. D., Sigman, D. M. & Haug, G. H. A pervasive link between Antarctic ice core and subarctic Pacific sediment records over the past 800 kyrs. *Quat. Sci. Rev.* **29**, 206–212 (2010).
70. Lo, L. et al. Precession and atmospheric CO₂ modulated variability of sea ice in the central Okhotsk Sea since 130,000 years ago. *Earth Planet. Sci. Lett.* **488**, 36–45 (2018).
71. Gorbarenko, S. A. et al. Responses of the Okhotsk Sea environment and sedimentology to global climate changes at the orbital and millennial scale during the last 350 kyr. *Deep Sea Res. Part II* **61–64**, 73–84 (2012).
72. Nürnberg, D. & Tiedemann, R. Environmental change in the Sea of Okhotsk during the last 1.1 million years. *Paleoceanography* **19**, 1–23 (2004).
73. Iwasaki, S. et al. Paleocceanography of the last 500 kyrs in the central Okhotsk Sea based on geochemistry. *Deep Sea Res. Part II* **61–64**, 50–62 (2012).
74. Wan, S., Li, A., Clift, P. D. & Stuut, J. B. W. Development of the East Asian monsoon: mineralogical and sedimentologic records in the northern South China Sea since 20 Ma. *Palaeogeogr. Palaeoclimatol. Palaeoecol.* **254**, 561–582 (2007).
75. Biscaye, P. E. Mineralogy and sedimentation of recent deep-sea clay in the Atlantic Ocean and adjacent seas and oceans. *Geol. Soc. Am. Bull.* **76**, 803–832 (1965).
76. Lu, Z., Liu, Z., Chen, G. & Guan, J. Prominent precession band variance in ENSO intensity over the last 300,000 years. *Geophys. Res. Lett.* **46**, 9786–9795 (2019).
77. Peltier, W. R. Global glacial isostasy and the surface of the ice-age earth: the Ice-5G (VM2) model and GRACE. *Annu. Rev. Earth Planet. Sci.* **32**, 111–149 (2004).
78. Otto-Bliesner, B. L. et al. Last glacial maximum and Holocene climate in CCSM3. *J. Clim.* **19**, 2526–2544 (2006).
79. Yeager, S. G., Shields, C. A., Large, W. G. & Hack, J. J. The low-resolution CCSM3. *J. Clim.* **19**, 2545–2566 (2006).
80. Hammer, Ø., Harper, D. A. & Ryan, P. D. PAST: paleontological statistics software package for education and data analysis. *Palaeontol. Electron.* **4**, 9 (2001).
81. Howell, P., Pisis, N., Ballance, J., Baughman, J. & Ochs, L. *ARAND Time-Series Analysis Software* (Brown University, 2006).
82. Li, M., Hinnov, L. & Kump, L. Acycle: time-series analysis software for paleoclimate research and education. *Comput. Geosci.* **127**, 12–22 (2019).
83. Grinsted, A., Moore, J. C. & Jevrejeva, S. Application of the cross wavelet transform and wavelet coherence to geophysical time series. *Nonlinear Process. Geophys.* **11**, 561–566 (2004).

Acknowledgements

We thank the ship crew and other participants for their assistance during cruise LV55. We are grateful to Prof. Shiming Wan, Dr. Jin Zhang, and Dr. Hualong Jin for their assistance in clay mineral analysis, and Dr. Aimei Zhu and Xiaojing Wang for their assistance with the ICP-OES and ICP-MS analyses. We thank Prof. Fuqing Jiang, Dr. Benhong Guo, Dr. Lijuan Lu, and Dr. Ruxi Dou for their helpful discussion and suggestions. This work was funded by the Laoshan Science and Technology Innovation Project (Grant No: LSKJ202204203), the National Natural Science Foundation of China (Grant Nos: 42276079, 42130412, and 42274094), the National Key Research and Development

Program of China (Grant No: 2023YFF0804600), the Taishan Scholar Program of Shandong (Grant No: tspd 20181216), Basic Scientific Fund for National Public Research Institutes of China (Grant No: GY0223G01), Shandong Provincial Natural Science Foundation (Grant No: ZR2024QD107). Additional funding was provided by the Swedish Research Council Vetenskapsrådet (Grant No: 2022-03617 to Z.L.) to Z.L. The transient simulation was analyzed on resources provided by the National Academic Infrastructure for Supercomputing in Sweden (NAISS, projects 2023/5-241 & SWESTORE) at Linköping University.

Author contributions

X.F. initiated this study and performed the laboratory measurements and data analysis. X.S. organized the cruise and sample collection, designed the study process, and obtained funding. Z.L. analyzed the 240 ka transient climate model simulation. H.C. contributed to the discussion and commented on the manuscript. X.F., J.Z., X.S., Z.L., H.C., Y.Z., Z.Y., Z.Y., H.L., Z.D., D.Z., H.F., J.D. and K.W. contributed to the refinement and revision of the paper.

Competing interests

The authors declare no competing interests.

Additional information

Supplementary information The online version contains supplementary material available at <https://doi.org/10.1038/s41612-025-01079-9>.

Correspondence and requests for materials should be addressed to Xuefa Shi or Zhengyao Lu.

Reprints and permissions information is available at <http://www.nature.com/reprints>

Publisher's note Springer Nature remains neutral with regard to jurisdictional claims in published maps and institutional affiliations.

Open Access This article is licensed under a Creative Commons Attribution-NonCommercial-NoDerivatives 4.0 International License, which permits any non-commercial use, sharing, distribution and reproduction in any medium or format, as long as you give appropriate credit to the original author(s) and the source, provide a link to the Creative Commons licence, and indicate if you modified the licensed material. You do not have permission under this licence to share adapted material derived from this article or parts of it. The images or other third party material in this article are included in the article's Creative Commons licence, unless indicated otherwise in a credit line to the material. If material is not included in the article's Creative Commons licence and your intended use is not permitted by statutory regulation or exceeds the permitted use, you will need to obtain permission directly from the copyright holder. To view a copy of this licence, visit <http://creativecommons.org/licenses/by-nc-nd/4.0/>.

© The Author(s) 2025